

# Temperature-driven structural phase transitions in SmNiO<sub>3</sub>: insights from deep potential molecular dynamics simulations

Guoyong Shi,<sup>1</sup> Fenglin Deng,<sup>2,3</sup> Ri He,<sup>4,5</sup> Dachuan Chen,<sup>6</sup> Xuejiao Chen,<sup>7</sup> Peiheng Jiang,<sup>1,\*</sup> and Zhicheng Zhong<sup>2,3,†</sup>

<sup>1</sup> *School of Physics, MOE Key Laboratory for Nonequilibrium Synthesis and Modulation of Condensed Matter, Xi'an Jiaotong University, Xi'an 710049, China*

<sup>2</sup> *School of Artificial Intelligence and Data Science, University of Science and Technology of China, Hefei 230026, China*

<sup>3</sup> *Suzhou Institute for Advanced Research, University of Science and Technology of China, Suzhou 215123, China*

<sup>4</sup> *CAS Key Laboratory of Magnetic Materials and Devices & Zhejiang Province Key Laboratory of Magnetic Materials and Application Technology, Ningbo Institute of Materials Technology and Engineering, Chinese Academy of Sciences, Ningbo 315201, China*

<sup>5</sup> *College of Materials Science and Opto-Electronic Technology, University of Chinese Academy of Sciences, Beijing 100049, China*

<sup>6</sup> *Ningbo Institute of Digital Twin, Eastern Institute of Technology, Ningbo 315201, China*

<sup>7</sup> *School of Photoelectric Engineering, Changzhou Institute of Technology, Changzhou, Jiangsu, 213002, China*

The metal-insulator transition (MIT) in rare-earth nickelates exemplifies the intricate interplay between electronic correlations and lattice dynamics in quantum materials. This work focuses on SmNiO<sub>3</sub> as a prototypical system, employing molecular dynamics simulations based on a “hidden” magnetic potential model. Our simulations reveal two key findings. First, the structural phase transition in SmNiO<sub>3</sub> is intrinsically temperature-driven and occurs spontaneously via collective lattice distortions. Moreover, systematic high-pressure simulations demonstrate a distinct pressure dependence of the transition temperature, which decreases monotonically with increasing external hydrostatic pressure. These results provide atomistic insights into the cooperative mechanisms underlying the MIT and the interplay between structural distortions and electron correlation effects. The computational approach developed herein offers a generalizable framework for investigating complex phase transitions in correlated quantum materials.

\* [jiangph@xjtu.edu.cn](mailto:jiangph@xjtu.edu.cn)

† [zczhong@ustc.edu.cn](mailto:zczhong@ustc.edu.cn)

# I. Introduction

Perovskite nickelates,  $R\text{NiO}_3$  (where  $R$  represents rare-earth ions), are a cornerstone in the study of correlated electron physics, as the interplay among charge, spin, and lattice degrees of freedom leads to metal-insulator transitions (MITs) coupled with magnetic ordering [1-5]. In addition to their fundamental significance in quantum phase transitions, these materials exhibit technologically relevant properties for applications in nanoelectronics and spintronics, thereby motivating extensive investigations into their structure-property relationships [6-8].

The MIT in  $R\text{NiO}_3$  ( $R \neq \text{La}$ ) occurs simultaneously with a paramagnetic to an antiferromagnetic state and a reduction in structural symmetry from orthorhombic ( $Pbnm$ ) to monoclinic ( $P2_1/n$ ) [9-12]. This transition is characterized by bond disproportionation and a breathing distortion of  $\text{NiO}_6$  octahedra, which results in alternating large and short Ni-O bonds [13]. Mott and Hubbard originally addressed the transition from an itinerant to a localized electronic regime in the *Hubbard model* [14,15]. Early models attributed these phenomena to charge ordering between  $\text{Ni}^{2+}$  ( $d^8$ ) and  $\text{Ni}^{4+}$  ( $d^6$ ) sites [16], however, recent experimental and theoretical studies have proposed a ligand-hole-mediated mechanism involving disproportionation, represented as  $2(d^8L^1) \rightarrow (d^8) + (d^8L^2)$ , where  $L$  denotes an O  $2p$  hole [2,17-20]. Crucially, Mercy *et al.* demonstrated that oxygen octahedral rotations precondition the lattice for breathing-mode softening, thereby establishing a cooperative electron-lattice instability mechanism [21].

Despite recent advances, two significant challenges persist: (i) The relative

contributions of electronic correlations and lattice dynamics in driving MITs remain quantitatively unresolved; (ii) Conventional computational approaches struggle to achieve both quantum accuracy and capacity for finite-temperature and large-scale simulations. These limitations hinder the predictive modeling of nickelate phase transitions under realistic conditions.

To address these challenges, we employed machine-learned interatomic potentials with multiscale molecular dynamics (MD) to investigate  $\text{SmNiO}_3$ —a representative nickelate that displays a pronounced MIT near room temperature. Our approach circumvents the conventional trade-offs between accuracy and computational expense by training neural networks on spin-polarized density functional theory (DFT+U) datasets. Temperature-dependent MD simulations elucidate the physical mechanisms underlying the structural evolution of  $\text{SmNiO}_3$ . This computational framework not only resolves longstanding debates about nickelate MIT mechanisms but also provides generalizable insights for the design of oxide quantum materials.

## II. Method

The Vienna Ab initio Simulation Package (VASP) was used to perform density functional theory (DFT) calculations employing the Projector Augmented Wave (PAW) method to generate training sets[22-24]. The exchange correlation functional was treated using the generalized gradient approximation (GGA), as formulated by PBEsol [25]. The valence configurations were employed as following:  $5s^26s^25p^65d^1$  for Sm,  $3d^94s^1$  for Ni, and  $2s^22p^4$  for O. The DFT+ $U$  method with a Hubbard correction ( $U = 2.0$  eV) was applied to describe the  $3d$  orbitals of Ni [26]. The energy cutoff of 500 eV

was adopted for the plane-wave basis set. The Monkhorst-Pack k-point grid was optimized to sample the Brillouin zone with a grid spacing of  $0.16 \text{ \AA}^{-1}$  k-points [27]. Convergence was achieved using criteria  $10^{-5}$  eV/atom for total energy and  $0.01 \text{ eV/\AA}$  for ionic force. Both the ground state calculations and *ab initio* molecular dynamics (AIMD) simulations considered spin-polarization. We utilize the general Deep Potential Generator (DP-GEN) scheme [28], the DeepPot-SE [29], to generate the training datasets.

Supercells consisting of 40 atoms corresponding to the  $P2_1/n$  and  $Pbnm$  space group were initially constructed. Subsequently, each supercell was randomly perturbed by scaling the lattice translation vectors with a range of -3 to 3% and by applying relative atomic displacements within a range of -0.008 to 0.008  $\text{\AA}$ . Next, 5-steps of AIMD were performed for each distorted structure in the NVT ensemble at 50 K. A total of 400 ionic configurations (including energy and force) were obtained from the AIMD simulations. These data served as the initial training dataset for the DP-GEN loop.

During each DP-GEN loop training step, four Deep potential (DP) models were trained using randomly initialized neural network parameters. Each training step comprised 600,000 steps. The learning rate was initially set to  $1 \times 10^{-3}$  and decayed exponentially to  $5 \times 10^{-8}$  throughout the training process. The loss function prefactors for the energy, atomic force, and the virial tensor were set as follows:  $p_e^{start} = 0.02$ ,  $p_e^{limit} = 2$ ,  $p_f^{start} = 1000$ ,  $p_f^{limit} = 1$ ,  $p_v^{start} = 0$ , and  $p_v^{limit} = 0$ . A cutoff radius of  $6.0 \text{ \AA}$  and a smooth cutoff radius of  $2.0 \text{ \AA}$  were employed. The neural network

architecture comprised three hidden layers, each with 240 nodes.

During the exploration step of the DP-GEN loop, a single DP model is selected to investigate various structures of  $\text{SmNiO}_3$  in  $P2_1/n$  and  $Pbnm$  supercells using Deep Potential Molecular Dynamics (DPMD) with the LAMMPS package [30]. Molecular dynamics simulations are conducted within the isothermal-isobaric (NPT) ensemble over a temperature range of 50 - 600 K. At each DPMD step, a criterion is applied to select one of four models for spin-polarized DFT calculations, which are used to update the training dataset for subsequent DP-GEN iterations. The DP-GEN loop is considered converged when the agreement between DP and DFT-calculated atomic forces reaches a predefined threshold of 99%. MD simulations employ a time step of 1 fs, periodic boundary conditions in all directions, and the NPT ensemble.

### III. Results

Initially, we conducted a full geometry relaxation on 80-atom supercells of both  $P2_1/n$  and  $Pbnm$  phases as depicted in Figs. 1a and 1b. The  $P2_1/n$  phase, exhibiting T-type antiferromagnetic (AFM) ordering was described in Ref.[2], and the  $Pbnm$  phase, exhibiting ferromagnetic (FM) ordering. In the  $P2_1/n$  phase, two distinct Ni states emerged, accompanied by a breathing-mode distortion of the  $\text{NiO}_6$  octahedra, which were classified as expanded (“L”) and contracted (“S”) units. The respective volumes of L and S octahedral units are  $10.08 \text{ \AA}^3$  and  $9.06 \text{ \AA}^3$ , respectively. In contrast, the  $Pbnm$  phase exhibited a single, equivalent Ni state with uniformly  $\text{NiO}_6$  octahedra (“M”), each having a volume of  $9.60 \text{ \AA}^3$ . Energetically, the  $Pbnm$  phase was 3 meV per atom higher than the  $P2_1/n$  phase. Density of states (DOS) calculations for both phases (see Figs. 1c

and 1d) revealed that the insulating  $P2_1/n$  phase possesses a band gap of 474 meV, whereas the  $Pbnm$  phase displays metallic characteristics. These results suggest that the crystal structure and charge states are coupled.

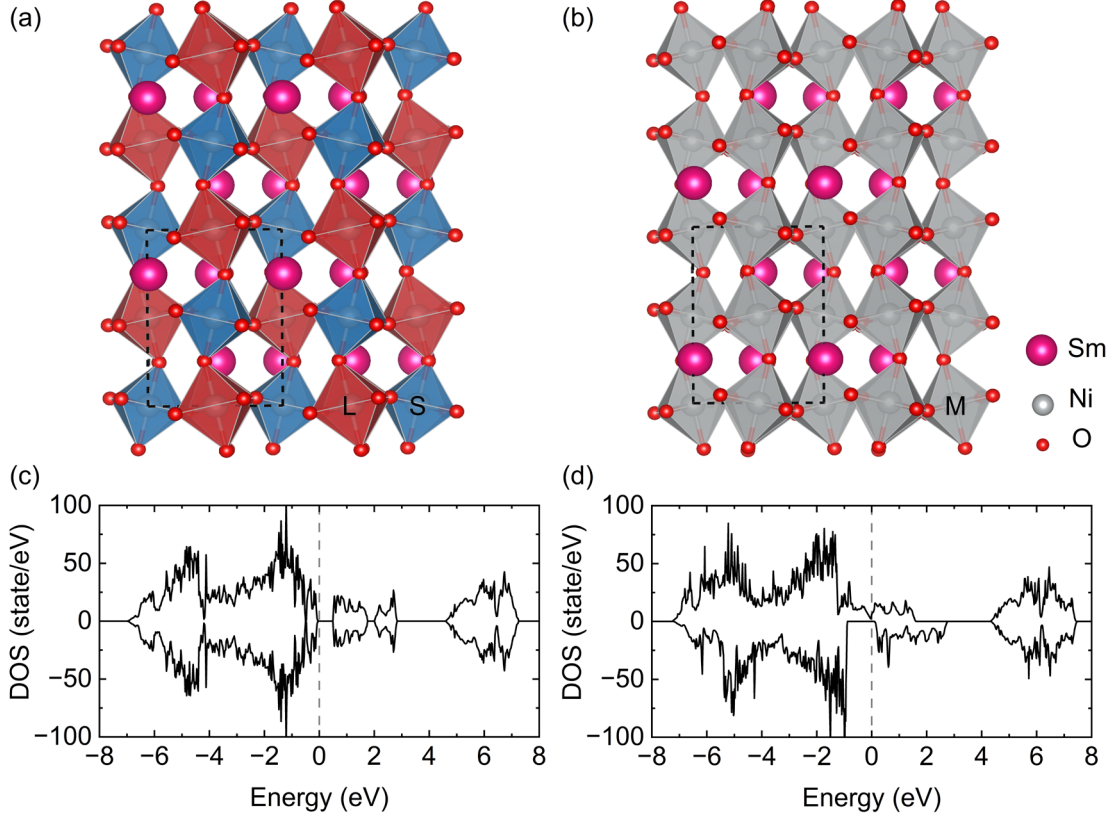


Fig. 1. Crystal structures of  $\text{SmNiO}_3$  in (a) the  $P2_1/n$  phase with T-type AFM ordering and (b) the  $Pbnm$  phase with FM ordering. Sm, Ni, and O atoms are represented by pink, grey, and red spheres, respectively. In the  $\text{NiO}_6$  octahedra of the  $P2_1/n$  phase, expanded (L) and contracted (S) units are color-coded as red and blue, respectively. In the  $\text{NiO}_6$  octahedra of the  $Pbnm$  phase, uniform (M) units are color-coded as grey. Density of states (DOS) for the  $P2_1/n$  and  $Pbnm$  phases are shown in panels (c) and (d), the Fermi energy set to 0 eV.

Based on these results, a DP model for  $\text{SmNiO}_3$  was constructed within a supervised machine learning framework. The training dataset included structural information, total energies, atomic forces, and virial tensors obtained from spin-polarized DFT calculations. Using the DP-GEN iterative procedure, the final dataset for potential development comprised 1429 configurations. A comparison of the energies

and forces predicted by the DP model with those computed via DFT reveals excellent agreement, as illustrated in Fig. 2. The root-mean-square errors (RMSE) for energy and force are 2.03 meV/atom and 84.74 meV/Å, respectively. Notably, the low RMSE values validate the accuracy of the interatomic potentials and the robustness of the training protocol.

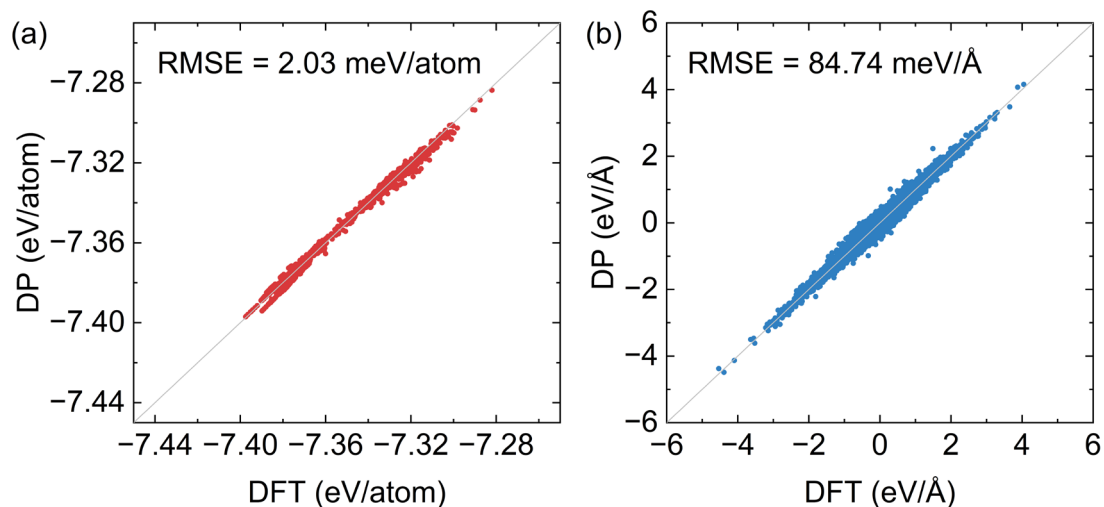


Fig. 2. Comparison of (a) total energies and (b) atomic forces between DFT and DP model calculations for SmNiO<sub>3</sub>.

After validating the potential model, MD simulations were performed on SmNiO<sub>3</sub> using a 7680-atom supercell. Fig. 3a demonstrates that at 50 K, the distance between the S and L curves indicates the persistence of the breathing-mode distortion characteristic of the low-temperature  $P2_1/n$  phase. The thermal evolution of the system is reflected in the progressive broadening of these curves, as shown in Fig. 3b, where enhanced thermal fluctuations cause a partial overlap between S and L features. Notably, at 320 K (Fig. 3c), although the peak separation between the S and L curves is substantially reduced, complete merging is not observed. This intermediate state suggests a partial suppression of the breathing distortion, accompanied by the initial

formation of regular  $\text{NiO}_6$  octahedra through heating. Upon further heating to 340 K (Fig. 3d), the complete coalescence of the S and L curves indicates the disappearance of the breathing-mode distortions, marking the structural transition to the centrosymmetric  $Pbnm$  phase. Our calculations indicate that the phase transition temperature between the  $P2_1/n$  and  $Pbnm$  phases is approximately 340 K, which is consistent with previous results [2].

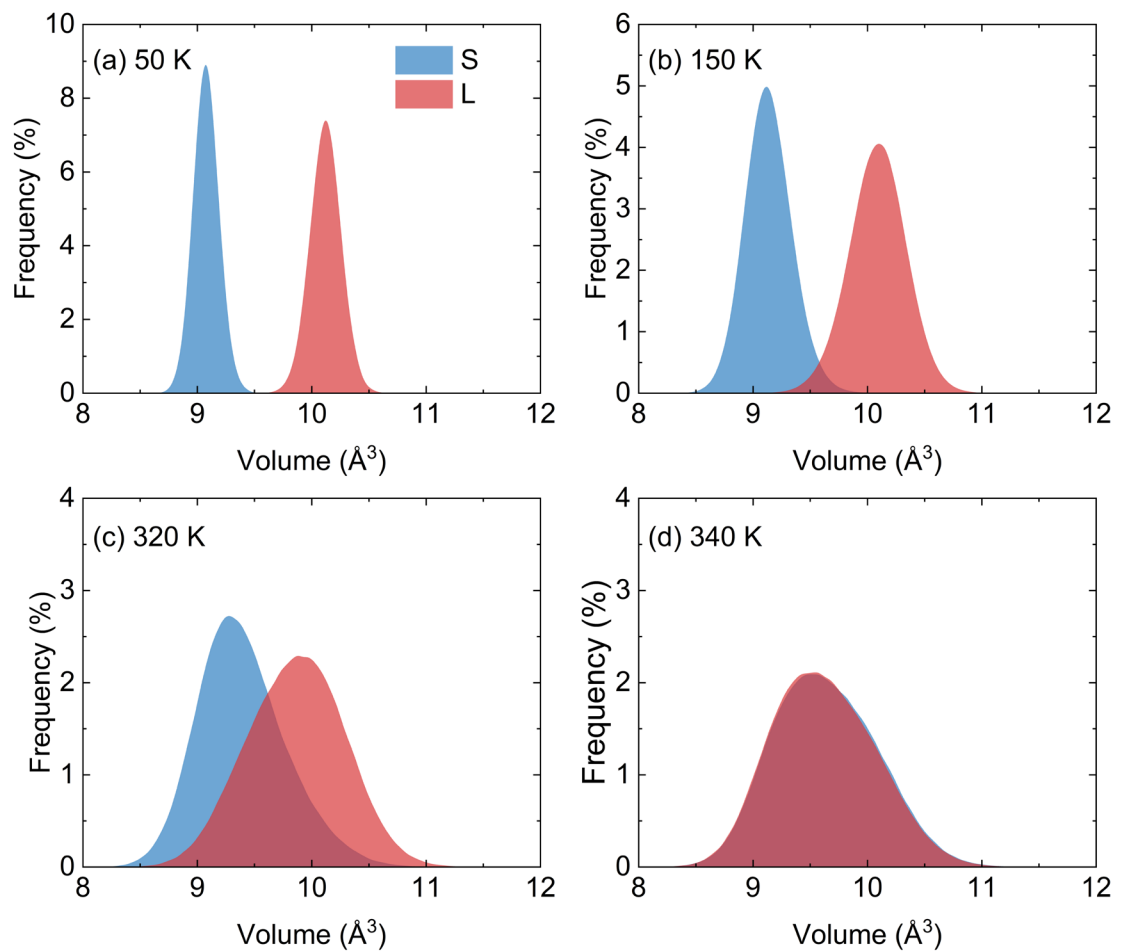


Fig. 3. The real-space distribution of S and L at (a) 50 K, (b) 250 K, (c) 320 K, and (d) 340 K.

To systematically investigate temperature-dependent structural evolution, we conducted crystallographic analysis by extracting final atomic configurations under varying thermal conditions and projecting them along the [001] crystallographic axis.



Fig. 4a shows that at 5 K, the NiO<sub>6</sub> octahedra adopt a well-ordered three-dimensional checkerboard arrangement characteristic of the breathing-mode distortion in the  $P2_1/n$  phase. This periodic modulation of octahedral sizes preserves long-range order at cryogenic temperatures. As the temperature increases to 150 K (Fig. 4b), the system maintains the essential breathing-mode structural signature despite slight variations in octahedral volumes, which indicate enhanced thermal fluctuations while maintaining the fundamental distortion pattern. At elevated temperatures near 500 K (Fig. 4c), our analysis reveals the complete loss of the characteristic octahedral size modulation. The difference between expanded and contracted octahedra becomes indistinguishable, with all NiO<sub>6</sub> units converging toward a uniform configuration. This thermal erasure of the breathing-mode distortion coincides with the reported monoclinic-to-orthorhombic structural transition in SmNiO<sub>3</sub>, thereby confirming the breakdown of long-range octahedral ordering at high temperatures through dynamic disordering processes.

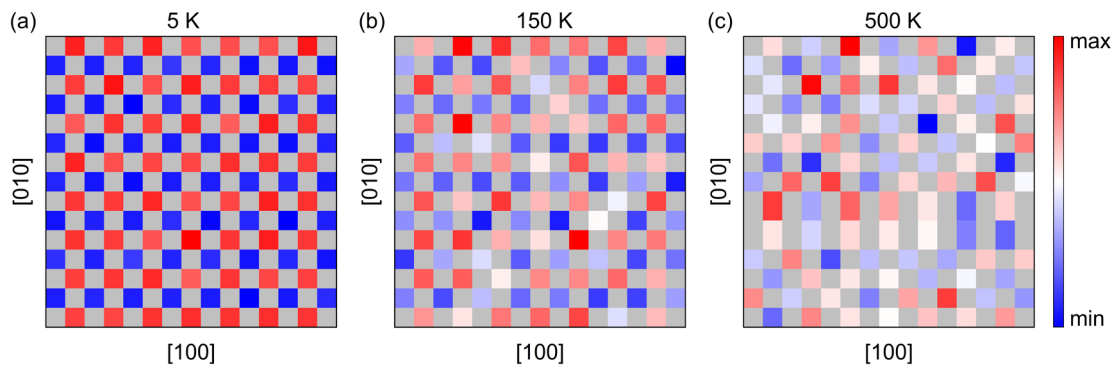


Fig. 4. Temperature-dependent evolution of NiO<sub>6</sub> octahedral dynamics revealed through molecular dynamics trajectories along the [001] crystallographic direction at (a)  $T = 5$  K, (b)  $T = 150$  K, and (c)  $T = 500$  K. Each marker corresponds to the real-space coordinates of a NiO<sub>6</sub> octahedron center, with data points color-mapped according to their instantaneous octahedral volume (right color scale).

Fig. 5 illustrates the temperature-dependent evolution of the volumes of two

distinct  $\text{NiO}_6$  octahedral units (designated as L and S), identified from the characteristic peaks in their respective distribution curves. At low temperatures, significant octahedral disproportionation is observed, with a marked volume contrast between the L and S units typical of the breathing-mode distorted  $P2_1/n$  phase. As the temperature increases, this structural disproportionation is progressively suppressed, as evidenced by the converging volume trajectories of the two octahedral species. This convergence indicates a structural transition to the centrosymmetric  $Pbnm$  phase, with 340 K established as the temperature for the symmetry-breaking transition. Notably, our molecular dynamics simulations employing a first-principles-trained machine learning interatomic potential decouple the electronic degrees of freedom from the structural evolution during phase transitions. These results demonstrate that the structural phase transition is the primary cause of MIT in  $\text{SmNiO}_3$ .

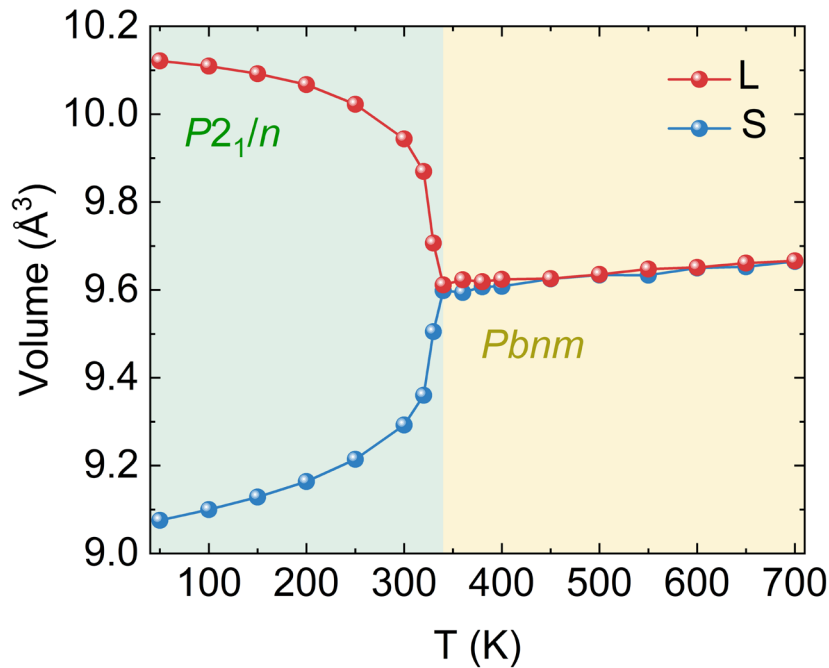


Fig. 5. Temperature-dependent evolution of octahedral unit volumes in  $\text{SmNiO}_3$ . The thermal variations of expanded (L, red curve) and contracted (S, blue curve)  $\text{NiO}_6$  octahedral volumes are displayed across the temperature range of 50-700 K.

Structural evolution under hydrostatic pressure offers an alternative pathway for modulating phase transitions in rare-earth nickelates [31,32]. To elucidate the pressure-dependent structural phase transition behavior of  $\text{SmNiO}_3$ , we performed MD simulations over a pressure range of 0-10 GPa using a DP model. The real-space distributions of the breathing-mode distortion parameters (S and L) at selected pressures (1, 3, 5, and 10 GPa) are systematically presented in Fig. 6. The corresponding phase transition temperatures were determined as 329 K (1 GPa), 316 K (3 GPa), 306 K (5 GPa), and 227 K (10 GPa), indicating a monotonic suppression of the transition temperature with increasing compression. Fig. 7 illustrates the constructed pressure-temperature phase diagram, which reveals a distinct negative slope ( $dT/dP < 0$ ) characterizing the pressure dependence of the structural phase transition. This trend is consistent with previous reports on  $R\text{NiO}_3$  systems by Zhou *et al.* [33], suggesting a universal mechanism underlying pressure effects in the  $R\text{NiO}_3$  family.

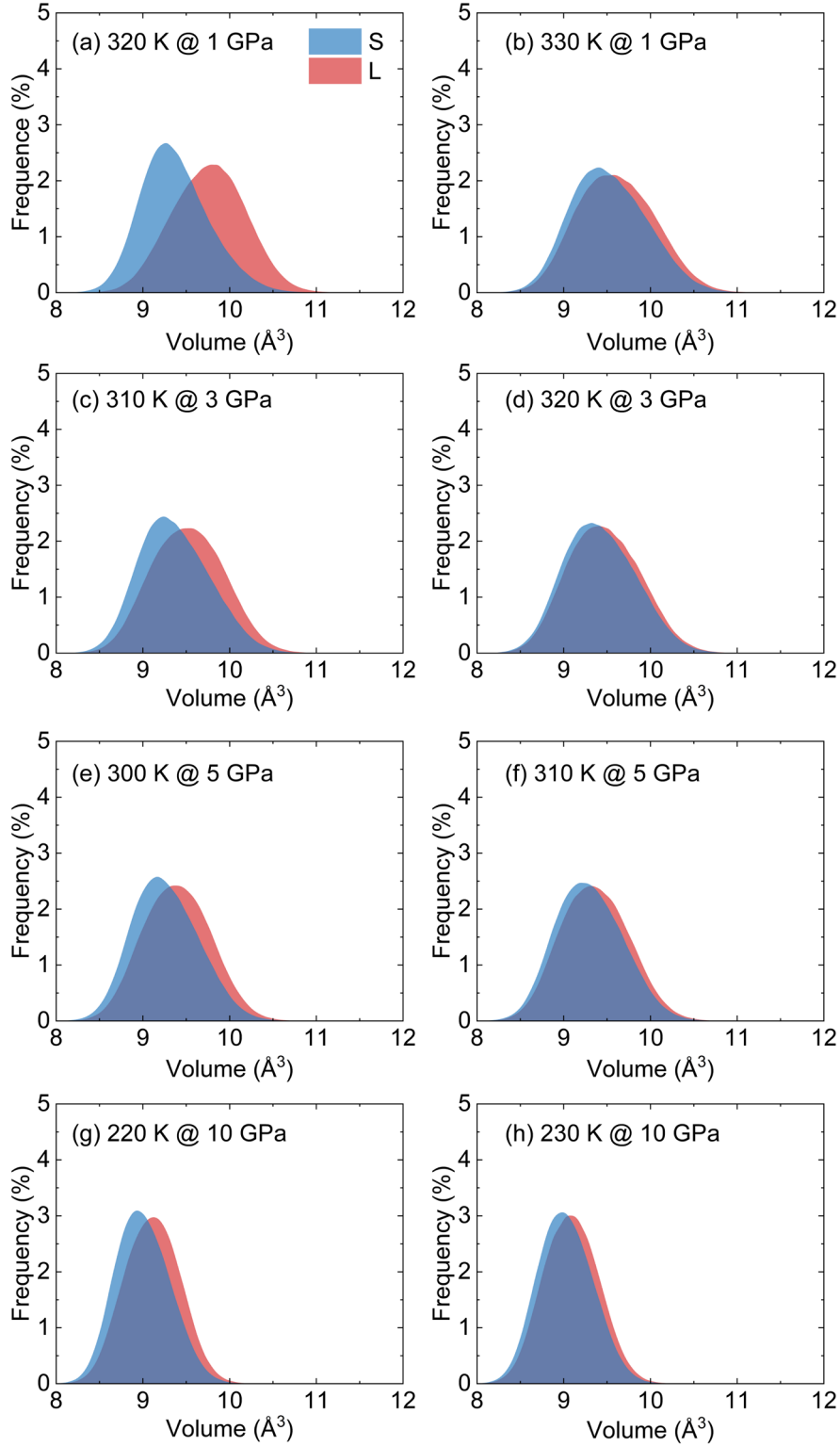


Fig. 6. The real-space distribution of S and L under (a)  $T = 320$  K and (b)  $T = 330$  K at 1 GPa; (c)  $T = 310$  K and (d)  $T = 320$  K at 3 GPa; (e)  $T = 300$  K and (f)  $T = 310$  K at 5 GPa; (g)  $T = 220$  K and (h)  $T = 230$  K at 10 GPa.

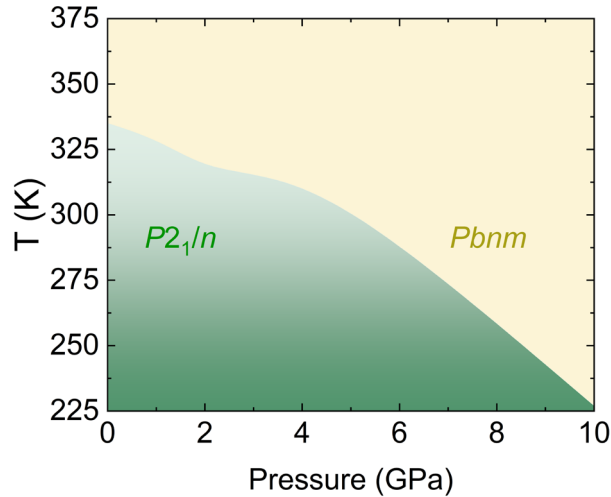


Fig. 7. Pressure-temperature (P-T) phase diagram of  $\text{SmNiO}_3$  across a comprehensive pressure range of 1-10 GPa.

## IV. Conclusions

In summary, we developed a machine-learning interatomic potential for  $\text{SmNiO}_3$  through deep neural network training, achieving first-principles accuracy. Utilizing the resulting DP model, we performed molecular dynamics simulations. Our results reveal the coexistence of two distinct  $\text{NiO}_6$  octahedral configurations with contrasting volumes in low-temperature  $\text{SmNiO}_3$  supercells. This bimodal distribution of  $\text{NiO}_6$  polyhedral evidences the characteristic breathing-mode distortion associated with the  $P2_1/n$  space group symmetry. Notably, the breathing-type structural modulation is progressively suppressed with increasing temperature, ultimately producing equivalent  $\text{NiO}_6$  units consistent with the conventional  $Pbnm$  phase at higher temperatures. Systematic analysis indicates a structural phase transition temperature of approximately 340 K, which is in excellent agreement with previous results. Furthermore, our finding demonstrates that hydrostatic pressure progressively reduces the phase transition temperature, establishing a clear pressure-dependent trend in the structural behavior of  $\text{SmNiO}_3$ .

## Acknowledgments

The authors acknowledge the financial support from the National Key R&D Program of China (Grants No. 2021YFA0718900 and No. 2022YFA1403000), the Key Research Program of Frontier Sciences of CAS (Grant No. ZDBS-LY-SLH008), the National Nature Science Foundation of China (Grants No. 12004400 and No. 12374096), and the China Fundamental Research Funds for the Central Universities.

## Reference

- [1] A. Hampel and C. Ederer, *Phys. Rev. B* **96**, 165130 (2017).
- [2] J. Varignon, M. N. Grisolia, J. Íñiguez, A. Barthélémy, and M. Bibes, *npj Quantum Mater.* **2**, 21 (2017).
- [3] S. Catalano, M. Gibert, J. Fowlie, J. Íñiguez, J. M. Triscone, and J. Kreisel, *Rep. Prog. Phys.* **81**, 046501 (2018).
- [4] Y. Lu, Z. Zhong, M. W. Haverkort, and P. Hansmann, *Phys. Rev. B* **95**, 195117 (2017).
- [5] D. I. Badrtdinov, A. Hampel, and C. E. Dreyer, *Phys. Rev. B* **104**, 054403 (2021).
- [6] Y. Cao, B. Lin, Y. Sun, H. Yang, and X. Zhang, *Electrochim. Acta* **174**, 41 (2015).
- [7] J. Shi, Y. Zhou, and S. Ramanathan, *Nat. Commun.* **5**, 4860 (2014).
- [8] S.-W. Cheong and M. Mostovoy, *Nat. Mater.* **6**, 13 (2007).
- [9] G. Catalan, *Phase Transitions* **81**, 729 (2008).
- [10] J. B. Torrance, P. Lacorre, A. I. Nazzari, E. J. Ansaldo, and C. Niedermayer, *Phys. Rev. B* **45**, 8209 (1992).
- [11] J. A. Alonso, M. J. Martínez-Lope, M. T. Casais, J. L. García-Muñoz, and M. T. Fernández-Díaz, *Phys. Rev. B* **61**, 1756 (2000).
- [12] J. A. Alonso, M. J. Martínez-Lope, M. T. Casais, M. A. G. Aranda, and M. T. Fernández-Díaz, *J. Am. Chem. Soc.* **121**, 4754 (1999).
- [13] J. A. Alonso, J. L. García-Muñoz, M. T. Fernández-Díaz, M. A. G. Aranda, M. J. Martínez-Lope, and M. T. Casais, *Phys. Rev. Lett.* **82**, 3871 (1999).
- [14] N. F. Mott, *Proc. Phys. Soc.* **62**, 416 (1949).
- [15] N. F. Mott, *Rev. Mod. Phys.* **40**, 677 (1968).
- [16] I. I. Mazin, D. I. Khomskii, R. Lengsdorf, J. A. Alonso, W. G. Marshall, R. M. Ibberson, A. Podlesnyak, M. J. Martínez-Lope, and M. M. Abd-Elmeguid, *Phys. Rev. Lett.* **98**, 176406 (2007).
- [17] H. Park, A. J. Millis, and C. A. Marianetti, *Phys. Rev. Lett.* **109**, 156402 (2012).
- [18] S. Johnston, A. Mukherjee, I. Elfimov, M. Berciu, and G. A. Sawatzky, *Phys. Rev. Lett.* **112**, 106404 (2014).
- [19] A. Subedi, O. E. Peil, and A. Georges, *Phys. Rev. B* **91**, 075128 (2015).

- [20] T. Mizokawa, D. I. Khomskii, and G. A. Sawatzky, *Phys. Rev. B* **61**, 11263 (2000).
- [21] A. Mercy, J. Bieder, J. Íñiguez, and P. Ghosez, *Nat. Commun.* **8**, 1677 (2017).
- [22] G. Kresse and J. Furthmüller, *Comput. Mater. Sci.* **6**, 15 (1996).
- [23] G. Kresse and J. Furthmüller, *Phys. Rev. B* **54**, 11169 (1996).
- [24] P. E. Blöchl, *Phys. Rev. B* **50**, 17953 (1994).
- [25] J. P. Perdew, A. Ruzsinszky, G. I. Csonka, O. A. Vydrov, G. E. Scuseria, L. A. Constantin, X. Zhou, and K. Burke, *Phys. Rev. Lett.* **100**, 136406 (2008).
- [26] A. I. Liechtenstein, V. I. Anisimov, and J. Zaanen, *Phys. Rev. B* **52**, R5467 (1995).
- [27] H. J. Monkhorst and J. D. Pack, *Phys. Rev. B* **13**, 5188 (1976).
- [28] Y. Zhang, H. Wang, W. Chen, J. Zeng, L. Zhang, H. Wang, and W. E, *Comput. Phys. Commun.* **253**, 107206 (2020).
- [29] L. Zhang, J. Han, H. Wang, W. A. Saidi, R. Car, and E. Weinan, End-to-end symmetry preserving inter-atomic potential energy model for finite and extended systems, in *Proceedings of the 32nd International Conference on Neural Information Processing Systems*, NIPS' 18 (Curran Associates, Inc., Red Hook, NY, 2018), pp. 4441-4451.
- [30] A. P. Thompson *et al.*, *Comput. Phys. Commun.* **271**, 108171 (2022).
- [31] X. Obradors, L. M. Paulius, M. B. Maple, J. B. Torrance, A. I. Nazzal, J. Fontcuberta, and X. Granados, *Phys. Rev. B* **47**, 12353 (1993).
- [32] P. C. Canfield, J. D. Thompson, S. W. Cheong, and L. W. Rupp, *Phys. Rev. B* **47**, 12357 (1993).
- [33] J. S. Zhou, J. B. Goodenough, and B. Dabrowski, *Phys. Rev. Lett.* **95**, 127204 (2005).